H/F substitution activating tunable dimensions and dielectric–optical properties in organic lead-bromide hybrids†

Lipeng Long,[a] Ziwen Huang,[a] Zhe-Kun Xu,[b] Tian Gan,[b] Yan Qin, [ID][b] Zhengwang Chen [ID][a] and Zhong-Xia Wang [ID] *[a]

Hybrid organic–inorganic halide perovskites as solution-processable semiconductors have progressed to be a promising class of optoelectronic materials. In this manuscript, we utilized H/F substitution to achieve structural dimension tailoring at the molecular level and tunable phase transition, dielectric, and optical features in organic lead-bromide hybrids, which have been rarely reported. The parent [piperidinium]PbBr$_3$ ([PD]PbBr$_3$) has a one-dimensional (1D) chain-like perovskite structure and shows successive solid–solid structural phase transitions. After monofluoride substitution, [4-FPD]$_6$Pb$_5$Br$_{16}$ (4-FPD = 4-fluoro-piperidinylaminium) presents a two-dimensional (2D) wave-like stacking and a significantly enhanced phase transition temperature, mainly attributed to the new C–F bonds generating extra inter-molecular interactions. Exceptionally, difluoride substituted [4,4-DFPD]$_2$PbBr$_4$ (4,4-DFPD = 4,4-difluoro-piperidinylaminium) with a 2D layered perovskite structure demonstrates interestingly irreversible to reversible structural phase transitions, accompanied by evident dielectric and nonlinear optical transformations. Moreover, the three hybrids show tunable semiconducting bandgaps and photoluminescence. This work provides great inspiration for the design of desired functional materials by rational chemical strategies and the intriguing properties of the new hybrids would also reveal promising applications in optoelectronic devices, data storage, etc.

Introduction

The recent progress in hybrid organic–inorganic halide perovskites (HOIHPs) showing extraordinary photovoltaic and appealing characteristics such as solution processability, structural diversity, strong optical absorption, *etc.* has been attracting a great deal of attention.[1–7] Such impressive performances and broad application prospects are mainly dependent on the integrated benefits of their flexible organic and functional inorganic components at the molecular level.[8,9] It is remarkable that the unfavorable tolerance factors in other hypothetical three-dimensional (3D) HOIHPs have prompted attempts to synthesize dimensionally reduced perovskites with higher structural tunability, greater stability, and more plentiful opto-

electronic properties.[10–14] Meanwhile, the abundant ingredients in different dimensional HOIHPs have also provided a great possibility to construct significant ferroic phase transition materials in condensed matter physical systems.[15–31] While witnessing the prosperity of HOIHPs, however, rational chemical modifications at the molecular level generating adjustable structures and physical properties still remain a challenge.

Benefitting from the inherent advantages of molecular materials, a variety of chemical tailoring and modifications could be applied to realize the targeted regulation of physical features. Very recently, H/F substitution has been actively pursued as a highly desirable strategy for advanced ferroelectrics and other phase transition materials.[32] The introduction of fluorine tends to significantly increase the phase transition temperature (T_c) and saturation polarization (P_s), attributed to its heavy mass and strong electronegativity. Compared to the well-known H/D isotope effect that is only efficacious in the proton displacement phase transition mechanism,[33–35] H/F substitution has shown a wider range of applications in most structural systems containing organic molecules. Moreover, fluoro-substitution also demonstrates considerable advantages of low toxicity and pretty good stability compared to deutera-

[a]College of Chemistry and Chemical Engineering, Gannan Normal University, Ganzhou 341000, People's Republic of China. E-mail: zhongxiawang@ncu.edu.cn
[b]Ordered Matter Science Research Center, Nanchang University, Nanchang 330031, People's Republic of China

This journal is © the Partner Organisations 2024

Inorg. Chem. Front., 2024, **11**, 845–852 | **845**

tion. To be specific, monofluoride substitution in [1-azabicyclo [2.2.1]heptanea]CdCl$_3$ has received a record T_c enhancement of 229 K, which greatly surpasses that of 142 K in PbDPO$_4$ by the H/D isotope effect.[36] Besides, H/F substitution can also be applied to achieve rare homochiral ferroelectrics.[37,38] To overcome the limitations of selective fluorination, aromatic perfluorinated substitution was successfully carried out to design a new high-performance layered perovskite ferroelectric, showing a larger P_s and a higher T_c.[39] It should be noted that most of the reported fluoro-substituted products have the same structural stacking as their parents but there are also very few examples of significant structural variations after H/F substitution, leading to unexpected and exciting properties. For instance, a perovskite-type non-ferroelectric can be transformed to the rare antiperovskite ferroelectric by H/F substitution with the highest P_s and smaller coercivity field in antiperovskite ferroelectrics.[40] Fluorine substitution yields a dimension-increment perovskite showing an unprecedented ferroelectric domain vortex in molecular ferroelectrics.[41] Chemical modifications with fluorinated effects can effectively coordinate the relationship between the structure and performance to generate intriguing physical properties; however, the corresponding explorations are still slightly insufficient.

In this work, we report the application of fluoride substitutions to the organic cations of 1D [PD]PbBr$_3$ to receive dimension-increased 2D lead-bromide hybrid crystals, [4-FPD]$_6$Pb$_5$Br$_{16}$ and [4,4-DFPD]$_2$PbBr$_4$ (see Scheme 1). [PD]PbBr$_3$ possesses a classic ABX$_3$-type (A = monovalent organic cations; B = divalent metal cations; and X = halogen anions) perovskite structure containing infinite chains of face-sharing PbBr$_6$ octahedra and PD cations show an ordered arrangement in the skeletal spacer. [PD]PbBr$_3$ exhibits sequential structural phase transitions with the prominent dynamic motions of PD cations in response to temperature changes. [4-FPD]$_6$Pb$_5$Br$_{16}$ has a 2D wave-like stacking layer and can be viewed as a coalition of 1D and 2D structures containing both face-sharing and corner-sharing PbBr$_6$ octahedra. Monofluoride substitution produ-

cing a dimensional increment might be attributed to the longer C–F bond in the organic molecules, which gives new intramolecular interactions and increases the distance between organic cations. Besides, [4-FPD]$_6$Pb$_5$Br$_{16}$ exhibits high-temperature reversible phase transition behaviors and semiconductor properties. Interestingly, difluorinated [4,4-DFPD]$_2$PbBr$_4$ shows a 2D layered A$_2$BX$_4$-type perovskite packing configuration composed of infinite octahedral corner-sharing [PbBr$_4$]$_\infty^{2-}$ layers and organic parts with a lower bandgap than those of [4-FPD]$_6$Pb$_5$Br$_{16}$ and [PD]PbBr$_3$. Exceptionally, [4,4-DFPD]$_2$PbBr$_4$ undergoes irreversible to reversible phase transitions with heat with evident dynamic motions of the organic cation. Meanwhile, the phase transitions are accompanied by prominent changes in the dielectric and second-order nonlinear optical responses. Advanced H/F substitution for adjusting structural dimensions with new physical features is rarely reported. This finding would strongly encourage the development of a feasible route for desired functional materials by rational design. Moreover, the solid-state phase transition behaviors accompanied by the significant dielectric transition and optical response for the three hybrids show great promise in the applications of data storage, optical sensing, *etc.*
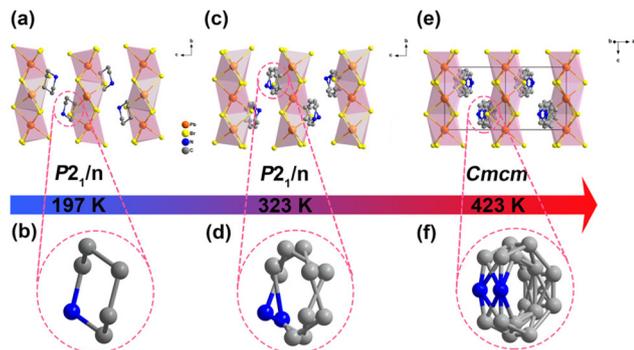
Results and discussion

[PD]PbBr$_3$

The synthesis and experimental details are described in the ESI.† The three hybrid crystals show well-verified phase purity and they have good thermal stability up to 480 K for possible practical applications (Fig. S1 and S2, ESI†). It is worth noting that [PD]PbBr$_3$ in this work has a 1D chain-like perovskite structure, which is different from that of the previously reported 2D layered perovskite [PD]$_2$PbBr$_4$, which exhibits disordered PD spacer cations in the interlayer and no detected thermal anomaly within the measurement range.[42] For [PD]PbBr$_3$, differential scanning calorimetry (DSC) records two pairs of reversible thermal anomalies at 404/398 K and 289/278 K, indicating that [PD]PbBr$_3$ exhibits sequential phase transitions (Fig. S3, ESI†). To figure out the mechanism, variable-temperature structural analyses were carried out. [PD]PbBr$_3$ crystallizes in a centrosymmetric monoclinic space group $P2_1/n$ at 197 K (Table S1, ESI†). As shown in Fig. 1a, the packing view presents 1D infinite chains composed of face-sharing [PbBr$_3$]$_\infty^-$ octahedra extending along the b-axis. The spaces between the chains are occupied by the PD cations stabilized *via* weak N–H⋯Br hydrogen bonding interactions (Fig. S4 and Table S2, ESI†). In this phase (low-temperature phase, LTP), the PD cation shows an ordered chair structure (Fig. 1b). With the increase of temperature to 323 K (intermediate-temperature phase, ITP), the cell parameter only shows slight volume expansion due to the thermal effect (Table S1, ESI†) and the PD cations exhibit an obviously disordered state caused by the disordered thermal motion of atoms (Fig. 1c and d). At 423 K (high-temperature phase, HTP), [PD]PbBr$_3$
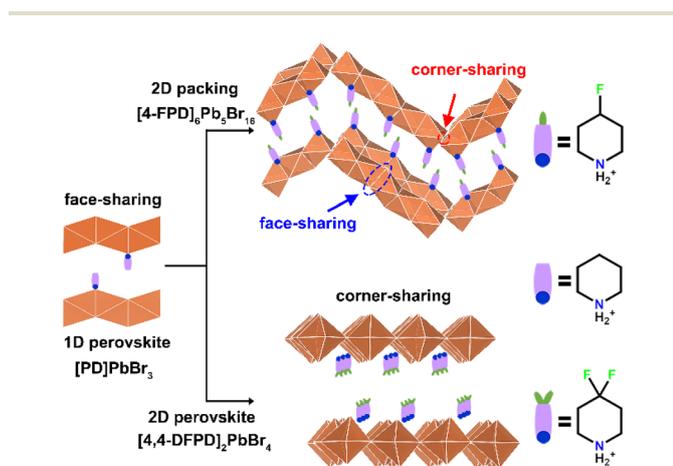
Scheme 1 Structural schematic diagram of [PD]PbBr$_3$, [4-FPD]$_6$Pb$_5$Br$_{16}$, and [4,4-DFPD]$_2$PbBr$_4$.

846 | *Inorg. Chem. Front.*, 2024, **11**, 845–852

This journal is © the Partner Organisations 2024

Fig. 1 Molecular structures of [PD]PbBr$_3$ at 197 K (a and b), 323 K (c and d), and 423 K (e and f). All the hydrogen atoms were omitted for clarity.

transfers to a higher symmetric orthorhombic *Cmcm* space group (Table S1, ESI†). The PD cation settles in a special mirror position, leading to its more highly disordered state (Fig. 1e and f). The obvious order–disorder motions of PD cations strongly confirm the structural phase transitions in [PD]PbBr$_3$. To further support the conclusion, we performed variable-temperature powder X-ray diffraction (V-PXRD) measurements. As depicted in Fig. S5 (ESI†), the PXRD patterns showed changes visible to the naked eye, and the number of peaks decreased appreciably in the color-marked regions from the LTP to HTP. For example, the double peaks at 18.59° and 32.03° in the LTP changed to two newly emerging single peaks at 18.38° and 31.77°, respectively, in the ITP. As the temperature continues to rise to the HTP, several double peaks (21.73° and 33.31°) in the ITP change to single peaks (21.57° and 33.05°) in the HTP. In terms of electrical properties, the dielectric constant commonly exhibits abrupt anomalies around T_c. As shown in Fig. S6 (ESI†), two successive dielectric anomalies appeared in a heating and cooling run, which are consistent with DSC and structural analysis results.

Monofluoride substituted [4-FPD]$_6$Pb$_5$Br$_{16}$

Through applying H/F substitution, unexpectedly, a 2D hybrid crystal [4-FPD]$_6$Pb$_5$Br$_{16}$ was obtained (Scheme 1). At 299 K, [4-FPD]$_6$Pb$_5$Br$_{16}$ has a monoclinic $P2_1/c$ space group (Table S1, ESI†). The stacking structure of [4-FPD]$_6$Pb$_5$Br$_{16}$ consists of both face-sharing and corner-sharing PbBr$_6$ octahedra constructing a wave-like 2D organic–inorganic hybrid structure, in which organic 4-FPD cations embedded in the inorganic layers (Fig. 2, upper). Significantly, in addition to the N–H···Br interactions, there is an even stronger C–H···F (2.41 Å) hydrogen bond between 4-FPD cations (Fig. S7 and Table S3, ESI†). Therefore, the obtained increase in dimensionality may be due to the repulsive effects created by new intermolecular interactions after H/F substitution. The organic 4-FPD cations settle in a general position and show an ordered state in the space between skeletons. As shown in Fig. S8 (ESI†), [4-FPD]$_6$Pb$_5$Br$_{16}$ exhibits very complex phase transition behaviors, in which the broad thermal anomaly including several peaks starts at 382 K and ends at 421 K in a heating run. Upon cooling, the thermal
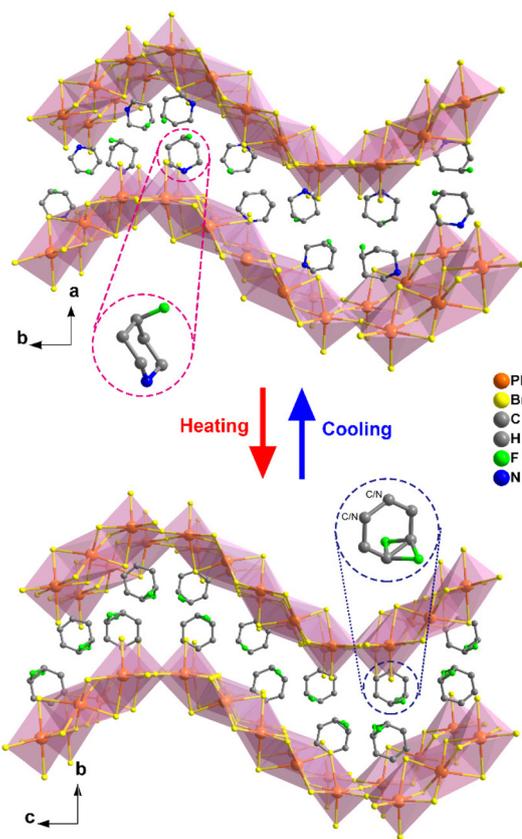
Fig. 2 Comparison of the packing structures of [4-FPD]$_6$Pb$_5$Br$_{16}$ at 299 K (upper) and 440 K (lower). All the hydrogen atoms were omitted for clarity.

condition shows a similar situation to that of the heating curve, revealing the occurrence of reversible phase transitions. The attempt to obtain clear single crystal structures of different phases failed and only the highest temperature phase was successfully collected. The ITP structure could not be obtained probably because of its phase structure instability. At 440 K, [4-FPD]$_6$Pb$_5$Br$_{16}$ crystallizes in an orthorhombic space group *Cmca* (Fig. 2, lower) and the cell parameters experience obvious changes (Table S1, ESI†). Moreover, the 4-FPD cations lay in a special position with mirror symmetry, leading to its highly disordered state. Upon cooling and heating, inorganic Br–Pb–Br bond angles and Pb–Br bond lengths of [4-FPD]$_6$Pb$_5$Br$_{16}$ in HTP have no evident changes compared to those in the LTP (Tables S4 and S5, ESI†). The varying crystal symmetry between phases with the disorder–order transition of 4-FPD cations confirms the structural phase transition in [4-FPD]$_6$Pb$_5$Br$_{16}$. To compensate for the lack of single crystal structures in the complex phase transitions, we performed V-PXRD measurements on [4-FPD]$_6$Pb$_5$Br$_{16}$. As plotted in Fig. S9 (ESI†), the spectral PXRD peaks shown in the black dotted line regions changed significantly upon heating. The apparent reduction of peaks implies an improvement in crystal symmetry, which is consistent with the crystal structure results. We also characterized its dielectric responses as shown in Fig. S10 (ESI†). The ε' presents a broad

This journal is © the Partner Organisations 2024

Inorg. Chem. Front., 2024, **11**, 845–852 | **847**

step-like transition from the LTP to HTP and exhibits a similar curve upon cooling.

Difluoride substituted [4,4-DFPD]₂PbBr₄

The difluoride substitution of $[4,4\text{-DFPD}]_2\text{PbBr}_4$ was also performed. $[4,4\text{-DFPD}]_2\text{PbBr}_4$ has a typical 2D layered perovskite structure. We first recognized its thermal phase transition behavior. As shown in Fig. 3, broad and complex endothermic peaks appear from 400 K to 430 K in the first round of heating (1st), but only an individual exothermic peak can be observed around 365 K upon the subsequent cooling. Then, we performed multiple rounds of DSC tests to observe the phase transition reversibility. Exceptionally, there is a new evident thermal anomaly peak around 396 K in the second heating and an exothermic peak around 362 K upon cooling (2nd). Then we performed two more rounds of DSC testing (3rd and 4th) and a pair of reversible thermal anomaly peaks at 395/362 K was recorded. Therefore, $[4,4\text{-DFPD}]_2\text{PbBr}_4$ underwent an obvious transformation from irreversible to stable reversible phase transitions when subjected to continuous heating and cooling tests. For convenience, we use different Greek letters to denote different phases as shown in Fig. 3.

Following the DSC results, variable-temperature single-crystal structures of $[4,4\text{-DFPD}]_2\text{PbBr}_4$ were characterized to reveal the structural changes. At 293 K, $[4,4\text{-DFPD}]_2\text{PbBr}_4$ crystallizes in a triclinic $P\bar{1}$ centrosymmetric space group, which was designated as the α phase (Table S6, ESI†). As seen in Fig. 4a and b, $[4,4\text{-DFPD}]_2\text{PbBr}_4$ contains ordered organic 4,4-DFPD cations occupying the cavity between the $[\text{PbBr}_4]_\infty^{2-}$ layers, in which the 4,4-DFPD cations are connected to the inorganic skeleton through weak N–H···Br interactions (Table S7, ESI†). As shown in Fig. S11 (ESI†), the 2D layered perovskite $[4,4\text{-DFPD}]_2\text{PbBr}_4$ possesses more complicated C–H···F hydrogen bonds existing between 4,4-DFPD cations
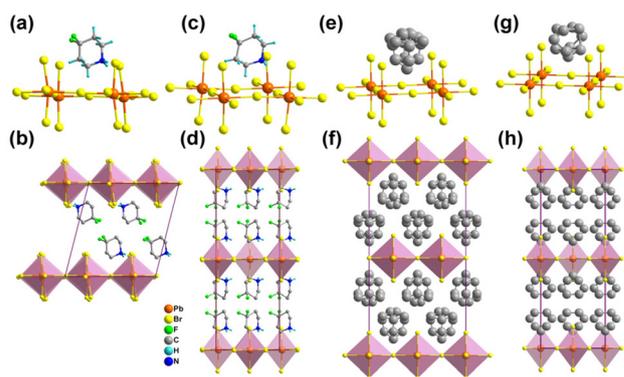
Fig. 4 Crystal structures and packing of $[4,4\text{-DFPD}]_2\text{PbBr}_4$. α phase at 293 K along the b-axis (a and b); δ phase at 293 K along the c-axis (c and d); λ phase at 420 K along the a-axis (e and f) and θ phase at 293 K along the a-axis (g and h), respectively. All the H atoms were omitted for clarity.

(Table S7, ESI†), which might have caused a completely different structural packing mode compared to the 1D perovskite $[\text{PD}]\text{PbBr}_3$ and 2D wave-like $[4\text{-FPD}]_6\text{Pb}_5\text{Br}_{16}$.

Upon heating to the β phase, we tried several times to obtain its single-crystal structure, but all failed. The possible reason is that the unstable structure leads to poor diffraction spots in the β phase. We only observed the most possible cell parameters with a tetragonal symmetry (β phase), which will be discussed below in the PXRD and nonlinear optics parts. Upon cooling to room temperature, $[4,4\text{-DFPD}]_2\text{PbBr}_4$ transfers to a noncentrosymmetric orthorhombic $Aea2$ space group (δ phase) (Table S6, ESI†). In Fig. 4c, the crystal structure remains the same as that of the α phase (Tables S8 and S9, ESI†). The difference is only that the number of layers in the unit cell doubles in the δ phase (Fig. 4d). When the crystal is heated again to the λ phase, $[4,4\text{-DFPD}]_2\text{PbBr}_4$ possesses a centrosymmetric space group $I4/mmm$ at 420 K (Table S6, ESI†). In Fig. 4e and f, the stacking of $[4,4\text{-DFPD}]_2\text{PbBr}_4$ does not change significantly, but the degree of PbBr_6 octahedral distortion is obviously reduced (Table S10, ESI†) and the organic 4,4-DFPD cations show a distinct spherically disordered state, which is due to the special four-fold axis symmetry operation. When cooled to 293 K, $[4,4\text{-DFPD}]_2\text{PbBr}_4$ attains the θ phase and has a centrosymmetric space group $Fmmm$ (Table S6, ESI†). As shown in Fig. 4g and h, the PbBr_6 octahedral shows a slight distortion (Table S11, ESI†), and the 4,4-DFPD cations remain in disordered states because of the special two-fold axis but show a certain degree of order, relative to the λ phase. We then continued to heat and freeze the $[4,4\text{-DFPD}]_2\text{PbBr}_4$ crystal for multiple rounds and found that the unit cell parameters remained as the space group $Fmmm$ in the LTP and $I4/mmm$ in the HTP, respectively. Obviously, $[4,4\text{-DFPD}]_2\text{PbBr}_4$ experienced a transformation process from irreversible ($P\bar{1} \rightarrow I\bar{4} \rightarrow Aea2 \rightarrow I4/mmm \rightarrow Fmmm$) to reversible ($Fmmm \rightarrow I4/mmm$) structural phase transitions.

The above exceptional structural phase transitions were also confirmed by V-PXRD measurements. As plotted in Fig. S12 (ESI†), we found that the spectrum of each phase is
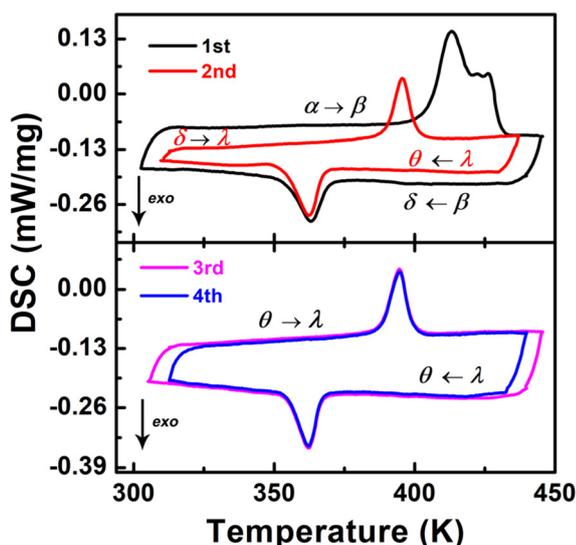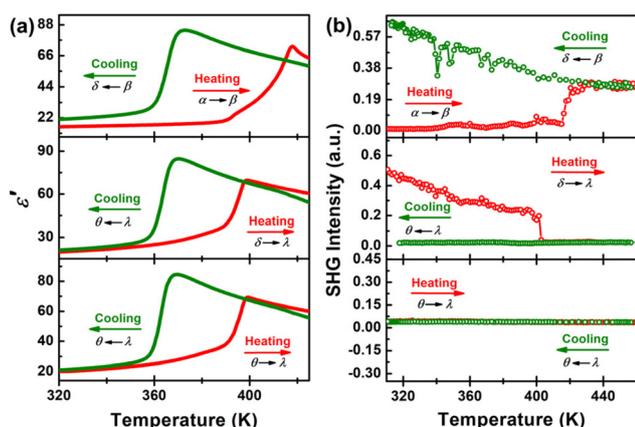

Fig. 3 DSC in several cycles upon heating and cooling for $[4,4\text{-DFPD}]_2\text{PbBr}_4$. The arrow of exo indicates the exothermic direction.

848 | *Inorg. Chem. Front.*, 2024, **11**, 845–852

This journal is © the Partner Organisations 2024

different, proving that $[4,4\text{-DFPD}]_2\text{PbBr}_4$ shows clear phase transition behaviors. Specifically, a new distinct peak appeared at 7.38° when the α phase was transferred to the β phase. Then, the evident PXRD peak at 20.15° in the β phase disappeared when the crystal was in the δ phase, showing two new weak peaks at 20.05° and 20.48°. The peaks around 28.50° also showed a visible reduction from the β phase to the δ phase, indicating that the symmetry of the δ phase is higher than that of the β phase. The patterns between λ and β phases, and θ and δ phases are very similar, and are attributed to the same crystallographic system that they belong to. Therefore, the β phase is tetragonal. The PXRD results agree well with the DSC and crystal structural analysis results.

Multiple successive rounds of temperature-dependent dielectric constant ε' testing following the DSC results are shown in Fig. 5a. The ε' value of $[4,4\text{-DFPD}]_2\text{PbBr}_4$ remains relatively stable at *ca.* 20 in the range of 320–380 K (upper). As the temperature continues to rise, a wide and complex peak-shaped anomaly is observed, in which the ε' value increases from *ca.* 20 to the peak maximum of *ca.* 73, being consistent with the appearance of the sequential exothermic peaks in the DSC curve (α to β). Upon cooling (β to δ), the ε' slowly rises to a maximum value of *ca.* 84 at 373 K and then experiences a significant step-like anomaly with the value sharply decreasing to *ca.* 28. In the 2nd heating–cooling cycle (middle), the ε' increases slowly with the temperature but shows a sudden step-like anomaly around 395 K with the value changing from *ca.* 20 to *ca.* 70 (δ to λ). In the cooling process (λ to θ), a similar step-like anomaly around 362 K to that in the 1st was observed. Obviously, the different dielectric anomalies in the 1st and 2nd heating–cooling cycles indicate the irreversible phase transition. When we performed the third round of dielectric testing (3rd), we found that the ε' appears almost exactly the same as that in the 2nd round, revealing the reversible feature (lower). Therefore, the temperature-dependent dielectric constant results also indicate that $[4,4\text{-DFPD}]_2\text{PbBr}_4$ experienced irreversible to reversible phase transitions.
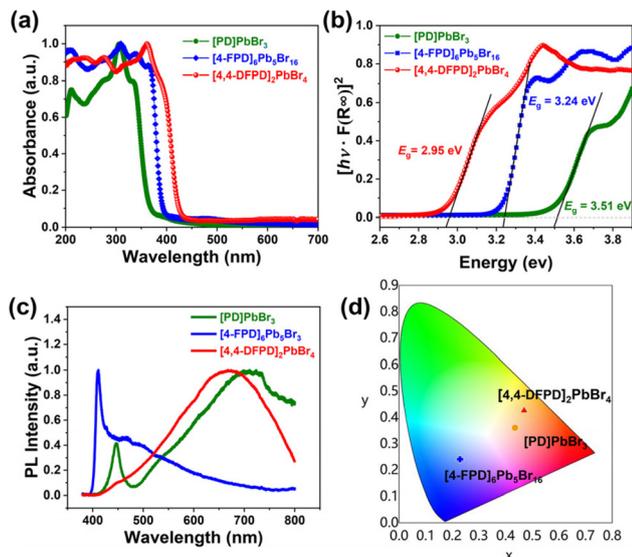
During these complex phase transitions, single-crystal structural analyses of $[4,4\text{-DFPD}]_2\text{PbBr}_4$ reveal that the β and δ phases belong to noncentrosymmetric space groups. Therefore, the variation of SHG signal intensity is expected for the symmetry changes involving polar space groups that usually exhibit nonlinear optical properties.[43,44] As shown in Fig. 5b, the SHG intensity in the initial state is zero, corresponding to the $P\bar{1}$ centrosymmetric space group (upper). When the sample was continuously heated to around 400 K, the SHG signal presented a jump-like change with the value soaring to *ca.* 0.25 V, strongly pointing to a polar structure in the β phase. Although no abrupt changes were observed in the next cooling process, the SHG signal slowly increased from 0.25 V to 0.6 V, implying that the SHG intensity in the δ phase ($Aea2$) is stronger than that in the β phase. The polar feature confirmed by SHG also supports the results of crystal structure analyses. Upon continuous heating (middle), the intensity of the SHG signal shows a sudden drop from a non-zero value to zero around 395 K, denoting that the crystal symmetry experienced a significant change from a non-centrosymmetric to centrosymmetric form (δ to λ). Then, the SHG signal remains at zero in the cooling process and reveals that a crystal symmetry variation occurs from centrosymmetric to centrosymmetric, agreeing well with the structural transition between the λ phase ($I4/mmm$) to the θ phase ($Fmmm$). In the 3rd heating and cooling cycle (lower), the intensity of SHG retains the zero state, consistent with the reversible phase transition referring to centrosymmetric space groups both in the LTP and HTP. Therefore, the change of the SHG signal with temperature strongly indicates that $[4,4\text{-DFPD}]_2\text{PbBr}_4$ undergoes irreversible to reversible structural phase transitions, in agreement with single crystal structure analysis results.

Semiconducting and photoluminescence properties

Lead-bromide hybrids are expected to be potential optical semiconductors showing luminescence, and their solid-state UV absorption and fluorescence spectra were recorded.[45] As depicted in Fig. 6a and b, their experimental band gaps mainly contributed by the inorganic framework were calculated to be 3.51 eV, 3.24 eV, and 2.95 eV for $[\text{PD}]\text{PbBr}_3$, $[4\text{-FPD}]_6\text{Pb}_5\text{Br}_{16}$, and $[4,4\text{-DFPD}]_2\text{PbBr}_4$, respectively, indicating their tunable semiconducting bandgaps. Besides, their photoluminescence properties also demonstrate significant differences. As shown in Fig. 6c, the fluorescence spectra of all three hybrids with similar broadband features were detected under 325 nm excitation such as a medium narrow emission at 446 nm and a broadband emission in $[\text{PD}]\text{PbBr}_3$, a strong narrow emission at 410 nm and a weak broad tail in $[4\text{-FPD}]_6\text{Pb}_5\text{Br}_{16}$, and a negligible peak at 446 nm and a strong broadband emission in $[4,4\text{-DFPD}]_2\text{PbBr}_4$. The broadband emission denotes the formation of self-trapped excitons due to structural distortion. However, the trap depth is indeed different due to the diverse structural dimensionalities and octahedral connectivity, resulting in the distinct population of free excitons and self-trapped excitons and hence diverse photoluminescence emissions.[46–48] The color coordinates of their

Fig. 5 Temperature-dependence of ε' (a) and SHG signal intensity (b) of the $[4,4\text{-DFPD}]_2\text{PbBr}_4$ powder sample measured in three successive heating–cooling cycles.

Fig. 6 (a) UV absorption spectra; (b) the Tauc plot; (c) photo-luminescence spectra; and (d) color coordinates on the CIE 1931 color space.

emissions are plotted on the CIE 1931 color space (Fig. 6d), implying their diverse luminescence properties.

Conclusions

In summary, we have fabricated three new hybrid crystals [PD]PbBr$_3$, [4-FPD]$_6$Pb$_5$Br$_{16}$, and [4,4-DFPD]$_2$PbBr$_4$. It was found that fluorination not only significantly increases the dimensionality from 1D to 2D, but also regulates their phase transitions and dielectric and optical properties. The introduction of the fluorine atom gives a longer C–F bond and new weak intermolecular interactions, which possibly makes a significant impact on the structural dimension tailoring. Consequently, the physical properties also undergo evident changes in response to structural changes. Monofluoride substituted 2D hybrid [4-FPD]$_6$Pb$_5$Br$_{16}$ shows higher T_c compared to the parent 1D perovskite [PD]PbBr$_3$. Interestingly, the 2D layered perovskite [4,4-DFPD]$_2$PbBr$_4$ exhibits exceptionally and interestingly irreversible to reversible phase transition behaviors accompanied by optoelectronic transformations. Besides, all three hybrids exhibit semiconducting characteristics with tunable bandgaps and photoluminescence. The new hybrids show application potential in optoelectronic devices, data storage, *etc.* This finding expands the pathway to constructing new desired functional materials based on rational chemical design.

Experimental

Synthesis and methods

All the reagents and solvents purchased were of reagent grade and used without further purification. The details of synthesis

and experimental methods including single-crystal X-ray crystallography, DSC, PXRD, dielectric testing, UV-vis spectroscopy, and fluorescence spectroscopy are provided in the ESI.†

Author contributions

L. L. and Z.-K. X. synthesized the samples. Z. H., T. G., Y. Q., and Z. C. carried out the general characterization studies. Z.-X. W. conceived the study and wrote the manuscript with input from other authors.

Conflicts of interest

There are no conflicts to declare.

Acknowledgements

References

1 L. Mao, J. Chen, P. Vishnoi and A. K. Cheetham, The Renaissance of Functional Hybrid Transition-Metal Halides, *Acc. Mater. Res.*, 2022, **3**, 439–448.
2 A. Younis, C. H. Lin, X. W. Guan, S. Shahrokhi, C. Y. Huang, Y. T. Wang, T. Y. He, S. Singh, L. Hu, J. R. D. Retamal, J. H. He and T. Wu, Halide Perovskites: A New Era of Solution-Processed Electronics, *Adv. Mater.*, 2021, **33**, 2005000.
3 J. Y. Kim, J. W. Lee, H. S. Jung, H. Shin and N. G. Park, High-Efficiency Perovskite Solar Cells, *Chem. Rev.*, 2020, **120**, 7867–7918.
4 A. K. Jena, A. Kulkarni and T. Miyasaka, Halide Perovskite Photovoltaics: Background, Status, and Future Prospects, *Chem. Rev.*, 2019, **119**, 3036–3103.
5 F. P. G. de Arquer, A. Armin, P. Meredith and E. H. Sargent, Solution-processed semiconductors for next-generation photodetectors, *Nat. Rev. Mater.*, 2017, **2**, 16100.
6 J. S. Manser, J. A. Christians and P. V. Kamat, Intriguing Optoelectronic Properties of Metal Halide Perovskites, *Chem. Rev.*, 2016, **116**, 12956–13008.
7 T. M. Brenner, D. A. Egger, L. Kronik, G. Hodes and D. Cahen, Hybrid organic-inorganic perovskites: low-cost semiconductors with intriguing charge-transport properties, *Nat. Rev. Mater.*, 2016, **1**, 15007.
8 W. Li, Z. M. Wang, F. Deschler, S. Gao, R. H. Friend and A. K. Cheetham, Chemically diverse and multifunctional hybrid organic-inorganic perovskites, *Nat. Rev. Mater.*, 2017, **2**, 16099.

9 B. Saparov and D. B. Mitzi, Organic-Inorganic Perovskites: Structural Versatility for Functional Materials Design, *Chem. Rev.*, 2016, **116**, 4558–4596.

10 C. K. Zhou, H. R. Lin, Q. Q. He, L. J. Xu, M. Worku, M. Chaaban, S. Lee, X. Q. Shi, M. H. Du and B. W. Ma, Low dimensional metal halide perovskites and hybrids, *Mater. Sci. Eng., R*, 2019, **137**, 38–65.

11 L. L. Mao, C. C. Stoumpos and M. G. Kanatzidis, Two-Dimensional Hybrid Halide Perovskites: Principles and Promises, *J. Am. Chem. Soc.*, 2019, **141**, 1171–1190.

12 G. Grancini and M. K. Nazeeruddin, Dimensional tailoring of hybrid perovskites for photovoltaics, *Nat. Rev. Mater.*, 2019, **4**, 4–22.

13 P. Gao, A. B. Yusoff and M. K. Nazeeruddin, Dimensionality engineering of hybrid halide perovskite light absorbers, *Nat. Commun.*, 2018, **9**, 5028.

14 L. W. Tang, H. X. Chen, Y. Ma, Y. Liu, L. N. Hua, L. Lu, B. B. Wang, S. G. Han, Z. H. Sun and J. H. Luo, A bilayered two-dimensional hybrid perovskite with a cage-templated secondary cation for high efficiency photodetection, *Inorg. Chem. Front.*, 2022, **9**, 637–644.

15 T. Vijayakanth, D. J. Liptrot, E. Gazit, R. Boomishankar and C. R. Bowen, Recent Advances in Organic and Organic-Inorganic Hybrid Materials for Piezoelectric Mechanical Energy Harvesting, *Adv. Funct. Mater.*, 2022, **32**, 2109492.

16 S. Shahrokhi, W. X. Gao, Y. T. Wang, P. R. Anandan, M. Z. Rahaman, S. Singh, D. Y. Wang, C. Cazorla, G. L. Yuan, J. M. Liu and T. Wu, Emergence of Ferroelectricity in Halide Perovskites, *Small Methods*, 2020, **4**, 2000149.

17 R. Pandey, G. Vats, J. Yun, C. R. Bowen, A. W. Y. Ho-Baillie, J. Seidel, K. T. Butler and S. I. Seok, Mutual Insight on Ferroelectrics and Hybrid Halide Perovskites: A Platform for Future Multifunctional Energy Conversion, *Adv. Mater.*, 2019, **31**, 1807376.

18 T. Zhang, K. Xu, J. Li, L. He, D. W. Fu, Q. Ye and R. G. Xiong, Ferroelectric hybrid organic-inorganic perovskites and their structural and functional diversity, *Natl. Sci. Rev.*, 2023, **10**, nwac240.

19 Y. Y. Chen, C. H. Gao, T. Yang, W. J. Li, H. J. Xu and Z. H. Sun, Research Advances of Ferroelectric Semiconductors of 2D Hybrid Perovskites toward Photoelectronic Applications, *Chin. J. Struct. Chem.*, 2022, **41**, 2204001–2204011.

20 X. L. Liu, D. Li, H. X. Zhao, X. W. Dong, L. S. Long and L. S. Zheng, Inorganic-Organic Hybrid Molecular Materials: From Multiferroic to Magnetoelectric, *Adv. Mater.*, 2021, **33**, 2004542.

21 C. D. Liu, C. C. Fan, B. D. Liang, C. Y. Chai, C. Q. Jing, X. B. Han and W. Zhang, Spectrally Selective Polarization-Sensitive Photodetection Based on a 1D Lead-Free Hybrid Perovskite Ferroelectric, *ACS Mater. Lett.*, 2023, **5**, 1974–1981.

22 Y. M. Liu, K. Li, T. M. Guo, L. C. An, Z. Z. Zhang, M. H. Yu, W. Li and X. H. Bu, Ammonium Sulfate Structure-Type Hybrid Metal Halide Ferroelectric with Giant Uniaxial Spontaneous Strain, *ACS Mater. Lett.*, 2022, **4**, 1168–1173.

23 H. N. Zheng, R. R. Zhang, X. Wu, Q. H. Zhang, Z. Y. Wu, W. P. D. Wong, J. S. Chen, Q. H. Xu and K. P. Loh, Strain-Driven Solid-Solid Crystal Conversion in Chiral Hybrid Pseudo-Perovskites with Paramagnetic-to-Ferromagnetic Transition, *J. Am. Chem. Soc.*, 2023, **145**, 3569–3576.

24 J. Wang, Y. Ma, Z. Wang, X. Liu, S. Han, Y. Liu, W. Guo, J. Luo and Z. Sun, Unusual ferroelectric-dependent birefringence in 2D trilayered perovskite-type ferroelectric exploited by dimensional tailoring, *Matter*, 2022, **5**, 194–205.

25 Y. Peng, J. Bie, X. T. Liu, L. N. Li, S. Chen, W. Fa, S. S. Wang, Z. H. Sun and J. H. Luo, Acquiring High-T-C Layered Metal Halide Ferroelectrics via Cage-Confined Ethylamine Rotators, *Angew. Chem., Int. Ed.*, 2021, **60**, 2839–2843.

26 W. J. Xu, K. Romanyuk, J. M. G. Martinho, Y. Zeng, X. W. Zhang, A. Ushakov, V. Shur, W. X. Zhang, X. M. Chen, A. Kholkin and J. Rocha, Photoresponsive Organic-Inorganic Hybrid Ferroelectric Designed at the Molecular Level, *J. Am. Chem. Soc.*, 2020, **142**, 16990–16998.

27 C. C. Fan, X. B. Han, B. D. Liang, C. Shi, L. P. Miao, C. Y. Chai, C. D. Liu, Q. Ye and W. Zhang, Chiral Rashba Ferroelectrics for Circularly Polarized Light Detection, *Adv. Mater.*, 2022, **34**, 2204119.

28 T. T. Sha, Y. A. Xiong, Q. Pan, X. G. Chen, X. J. Song, J. Yao, S. R. Miao, Z. Y. Jing, Z. J. Feng, Y. M. You and R. G. Xiong, Fluorinated 2D Lead Iodide Perovskite Ferroelectrics, *Adv. Mater.*, 2019, **31**, 1901843.

29 W. F. Deng, Y. X. Li, Y. X. Zhao, J. S. Hu, Z. S. Yao and J. Tao, Inversion of Molecular Chirality Associated with Ferroelectric Switching in a High-Temperature Two-Dimensional Perovskite Ferroelectric, *J. Am. Chem. Soc.*, 2023, **145**, 5545–5552.

30 B. Q. Zhao, X. X. Chen, H. Ye, Y. P. Gong, J. Wang, L. Ye and W. X. Zhang, An anomalous ferroelastic phase transition arising from an unusual-conformational reversal of polar organic cations, *Chem. Sci.*, 2023, **14**, 5965–5973.

31 J. Q. Wang, G. Teri, H. F. Ni, Q. F. Luo, X. P. Wang, D. W. Fu, Y. Zhang and Q. Guo, Halogenation triggering rules in hybrid materials for fluorescence and dielectric phase transitions, *Inorg. Chem. Front.*, 2023, **10**, 3860–3866.

32 Y. Ai, H.-P. Lv, Z.-X. Wang, W.-Q. Liao and R.-G. Xiong, H/F substitution for advanced molecular ferroelectrics, *Trends Chem.*, 2021, **3**, 1088–1099.

33 C. Shi, X. Zhang, C. H. Yu, Y. F. Yao and W. Zhang, Geometric isotope effect of deuteration in a hydrogen-bonded host-guest crystal, *Nat. Commun.*, 2018, **9**, 481.

34 L. Sobczyk, M. Obrzud and A. Filarowski, H/D Isotope Effects in Hydrogen Bonded Systems, *Molecules*, 2013, **18**, 4467–4476.

35 A. Katrusiak and M. Szafranski, Ferroelectricity in NH center dot center dot center dot N hydrogen bonded crystals, *Phys. Rev. Lett.*, 1999, **82**, 576–579.

36 Y. Y. Tang, Y. F. Xie, Y. L. Zeng, J. C. Liu, W. H. He, X. Q. Huang and R. G. Xiong, Record Enhancement of Phase Transition Temperature Realized by H/F Substitution, *Adv. Mater.*, 2020, **32**, 2003530.

This journal is © the Partner Organisations 2024

Inorg. Chem. Front., 2024, **11**, 845–852 | **851**

37 J. X. Gao, W. Y. Zhang, Z. G. Wu, Y. X. Zheng and D. W. Fu, Enantiomorphic Perovskite Ferroelectrics with Circularly Polarized Luminescence, *J. Am. Chem. Soc.*, 2020, **142**, 4756–4761.

38 Y. Y. Tang, Y. Ai, W. Q. Liao, P. F. Li, Z. X. Wang and R. G. Xiong, H/F-Substitution-Induced Homochirality for Designing High-T_c Molecular Perovskite Ferroelectrics, *Adv. Mater.*, 2019, **31**, 1902163.

39 H. Y. Zhang, Z. X. Zhang, X. J. Song, X. G. Chen and R. G. Xiong, Two-Dimensional Hybrid Perovskite Ferroelectric Induced by Perfluorinated Substitution, *J. Am. Chem. Soc.*, 2020, **142**, 20208–20215.

40 Z. X. Wang, Y. Zhang, Y. Y. Tang, P. F. Li and R. G. Xiong, Fluoridation Achieved Antiperovskite Molecular Ferroelectric in $[(CH_3)_2(F-CH_2CH_2)NH]_3(CdCl_3)(CdCl_4)$, *J. Am. Chem. Soc.*, 2019, **141**, 4372–4378.

41 H. Y. Zhang, X. J. Song, X. G. Chen, Z. X. Zhang, Y. M. You, Y. Y. Tang and R. G. Xiong, Observation of Vortex Domains in a Two-Dimensional Lead Iodide Perovskite Ferroelectric, *J. Am. Chem. Soc.*, 2020, **142**, 4925–4931.

42 S. Q. Chai, J. B. Xiong, Y. S. Zheng, R. C. Shi and J. L. Xu, Dielectric phase transition of an A_2BX_4-type perovskite with a pentahedral to octahedral transformation, *Dalton Trans.*, 2020, **49**, 2218–2224.

43 P. P. Shi, Y. Y. Tang, P. F. Li, W. Q. Liao, Z. X. Wang, Q. Ye and R. G. Xiong, Symmetry breaking in molecular ferroelectrics, *Chem. Soc. Rev.*, 2016, **45**, 3811–3827.

44 K. Li, H. Ye, X. Q. Li, X. Q. Wang, J. H. Luo and X. T. Liu, Rational design of an organic-inorganic hybrid with Schiff base cations for an efficient quadratic nonlinear optical switch, *Inorg. Chem. Front.*, 2023, **10**, 435–442.

45 X. K. Liu, W. D. Xu, S. Bai, Y. Z. Jin, J. P. Wang, R. H. Friend and F. Gao, Metal halide perovskites for light-emitting diodes, *Nat. Mater.*, 2021, **20**, 10–21.

46 F. F. Gao, H. P. Song, Z. G. Li, Y. Qin, X. Li, Z. Q. Yao, J. H. Fan, X. Wu, W. Li and X. H. Bu, Pressure-Tuned Multicolor Emission of 2D Lead Halide Perovskites with Ultrahigh Color Purity, *Angew. Chem., Int. Ed.*, 2023, **62**, e202218675.

47 M. D. Smith and H. I. Karunadasa, White-Light Emission from Layered Halide Perovskites, *Acc. Chem. Res.*, 2018, **51**, 619–627.

48 L. L. Mao, P. J. Guo, M. Kepenekian, I. Hadar, C. Katan, J. Even, R. D. Schaller, C. C. Stoumpos and M. G. Kanatzidis, Structural Diversity in White-Light-Emitting Hybrid Lead Bromide Perovskites, *J. Am. Chem. Soc.*, 2018, **140**, 13078–13088.